Editors' Suggestion

Submicropulse electron-beam dynamics correlated with short-range wakefields in Tesla-type superconducting rf cavities

A. H. Lumpkin,* R. M. Thurman-Keup, D. Edstrom, and J. Ruan
Accelerator Division, Fermi National Accelerator Laboratory, Batavia, Illinois 60510, USA

(Received 31 January 2020; accepted 13 April 2020; published 4 May 2020)

We report direct observations of submicropulse beam centroid shifts (head-tail kicks) correlated with short-range wakefields generated by off-axis electron-beam steering in Tesla-type superconducting rf cavities. The experiments were performed at the Fermilab Accelerator Science and Technology (FAST) Facility using its unique configuration of a photocathode rf gun injecting beam into two separated nine-cell cavities. The cavities are in series with corrector magnets and beam position monitors (BPMs) located before, between, and after them. The off-axis steering in the cavity was guided by the rf BPM data and higher-order mode circuitry targeting the first and second dipole passbands. The centroid shifts of up to 300 μm from head to tail of the ~10-ps-long micropulses at 500 pC/b in a 3-MHz pulse train were measured via optical transition radiation at a downstream screen with a Hamamatsu C5680 synchroscan streak camera. We also showed that we could compensate such kicks from the first cavity with the short-range wakefields (SRWs) in the second cavity, and we observed the dilution of the beam size in the tail of the pulses. A simple numerical model of the SRW effect in a single Tesla cavity is compared to the experiment successfully. In principle, these fundamental results may be scaled to cryomodule configurations of major free-electron laser (FEL) facilities such as the European XFEL, Linac Coherent Light Source or LCLS-II XFEL, and the conceptual international linear collider.

DOI: 10.1103/PhysRevAccelBeams.23.054401

I. INTRODUCTION

An emittance growth of bright electron beams created by dipolar kicks of higher-order modes (HOMs) excited by beam offsets in the accelerating cavities represents a concern [1]. These long-range wakefields (LRWs) deflect portions of the pulse train or lead to submacropulse beam oscillations such as we previously reported in Tesla-type superconducting cavities [2]. Additionally, such off-axis steering generates short-range wakefields (SRWs) as seen in normal conducting L-band accelerators [3] and in S-band accelerators [4]. These SRWs lead to submicropulse transverse effects. In these earlier cases, the smaller bore of the cavities led to measurable effects for ~1-mm offsets when using a streak camera or spatial imaging of the transverse beam sizes. The accelerators for high-power x-ray free-electron laser (FEL) facilities such as the European XFEL [5] and the under-construction Linac Coherent Light Source-II (LCLS-II) x-ray FEL [6] are employing Tesla-type superconducting rf (SCRF) cavities. In the Tesla cavity with its larger bore of 70-mm diameter, the SRW effects are relatively smaller for a 1-mm beam offset, but they are still measurable at the 100-μm level. In our Tesla-type cavities, we show for the first time that the SRWs are more of a threat to emittance dilution than that of the HOMs or LRWs.

We report here submicropulse effects on beam transverse position centroids and time-slice sizes correlated with off-axis beam steering in Tesla-type cavities at the Fermilab Accelerator Science and Technology (FAST) Facility [7]. We used a 3-MHz micropulse repetition rate, a unique two-cavity configuration, and targeted diagnostics for these tests. Our initial data from an optical transition radiation (OTR) imaging source indicated that our streak camera can provide ~10-μm spatial resolution with 1–2 ps (σ) temporal resolution depending on the bandpass filter employed. Since the observed bunch lengths were 10–15 ps (σ), we had sufficient resolution for up to 20 time slices in the 4σ profile. Thus, we also obtained slice beam size and emittance information (when the Beta function is known). We relied on the HOM detectors and rf BPMs to assess the off-axis steering used to generate the SRW effects. We then used the streak camera to evaluate further the resulting beam dynamics. Our investigations address the following points: a search for centroid shifts *within* the ~10-ps-long micropulse, a search for SRW kick compensation by the second SCRF cavity, a search for possible slice-emittance effects, identification of a space-charge-dominated regime

*lumpkin@fnal.gov

and ellipsoidal beam, the distinguishing of the short-range wakefield centroid effect from the HOMs' submacropulse effect, and a comparison to a numerical model for short-range, transverse effects in a Tesla cavity.

II. EXPERIMENTAL ASPECTS

We present here the main aspects of the injector linac, the synchroscan streak camera, and the critical all-mirror optical transport features used in the experiments.

A. The FAST injector linac

The FAST linac is based on the L-band rf photocathode (PC) gun, which injects a beam at a 3-MHz micropulse or bunch (b) repetition rate into two SCRF capture cavities denoted CC1 and CC2, followed by transport to a low-energy electron spectrometer as shown in Fig. 1. The beam properties for the studies are shown in Table I. The total beam energy was 41 MeV with 4.5 MeV contributed by the gun and 20 and 17 MeV by the capture cavities, respectively. A Cs_2Te photocathode was irradiated by the UV component of the drive laser system described elsewhere [8]. The basic diagnostics for the studies include the rf BPMs (denoted as Bnnn) located before, between, and after the two cavities as well as downstream to the low-energy absorber (LEA) as shown in Fig. 1. These are supplemented by the imaging screens (denoted as Xnnn) at X107, X108, X121, and X124. The HOM couplers are located at the upstream (US) and downstream (DS) ends of each SCRF cavity, and these signals are processed by the HOM detector circuits with the output provided online though ACNET, the Fermilab accelerator controls network. The HOM detectors' bandpass filters were optimized for two dipole passbands from 1.6 to 1.9 GHz, and the 1.3-GHz fundamental was reduced with a notch filter. The rf BPM electronics were configured for bunch-by-bunch capability with reduced noise. At 2 nC per micropulse, the rms noise was found to be 25 μm in the horizontal axis (x) and 15 μm in the vertical axis (y) in B101 in the test with a 4.5-MeV beam from the gun. We reduced the noise effect by using 100-shot averages in the data at 500 pC/b. However, for these experiments on short-range transverse wakefields in CC1 and CC2, we relied on a streak camera to provide the submicropulse, spatiotemporal information as described in the next subsection. A cryomodule (CM) capable of contributing an additional 250 MeV to the beam energy is located downstream, but it was not used in these studies. Ten- to 20-shot averages were made using the streak-camera data to improve the statistical variances of the images, although the effects were visible in a single image.

TABLE I. Summary of the FAST electron-beam parameters used in the SRW studies.

Beam parameter	Units	Value
Micropulse charge	pC	100–1000
Micropulse repetition rate	MHz	3
Micropulse number		1–150
Transverse beam sizes (rms)	μm	100–1200
Transverse emittance, normalized	mm-mrad	2–5
Bunch length (rms)	ps	8–15
Energy, total	MeV	41
PC gun gradient	MV/m	40–45
CC1 gradient	MV/m	20
CC2 gradient	MV/m	17

B. The streak-camera system

We utilized a C5680 Hamamatsu streak camera as shown schematically in Fig. 2, with an S20 PC and M5675 synchroscan vertical deflection unit phase locked through a C6878 delay box to an 81.25-MHz clock derived from the 1.3-GHz rf master oscillator. This configuration stabilizes the streak image positions to ~1-ps temporal jitter over a comparatively long period (tens of minutes). These steps enabled the synchronous summing of 50–150 micropulses [or bunches (b)] generated at 3 MHz by the photoinjector and the offline summing of 10–100 images to improve statistics in the summed images. We applied this principle to OTR generated from an Al-coated Si substrate at the X121 screen location (see Fig. 1) with subsequent transport to the beam-line streak camera. Commissioning of the streak-camera system was facilitated through a suite of controls centered around ACNET. This suite included operational drivers to control and monitor the streak camera as well as graphical displays to facilitate the interface with the driver. Images were captured from the streak camera using the Prosilica 1.3-Mpixel readout camera with 2/3 "format, and these were analyzed both online and with an offline MATLAB-based ImageTool processing program based on fitting the slice and projected experimental

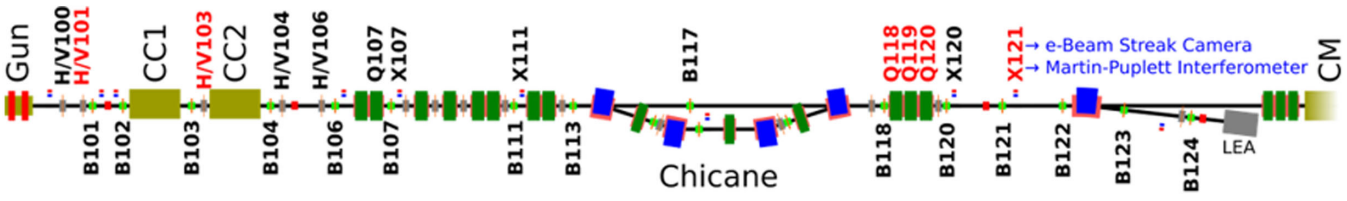

FIG. 1. Schematic of the FAST beam-line layout showing the capture cavities, correctors, rf BPMs, chicane, X121 OTR screen, spectrometer, and the beginning of the cryomodule (CM).

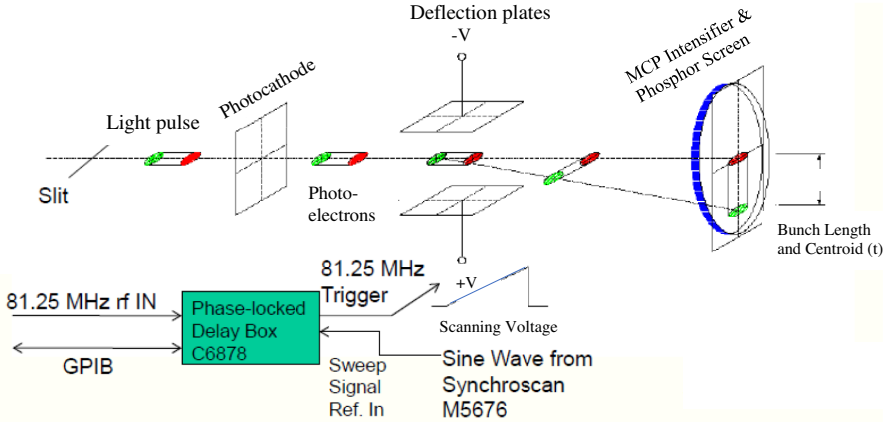

FIG. 2. Schematic of the streak-camera principles where the vertical axis is converted to a time axis with the ramped voltage on a set of deflection plates and timing is synchronized to an 81.25-MHz rf signal for picosecond phase stability. In this case, the head of the pulse (red) is undeflected, and the tail of the pulse (green) is deflected the most vertically downward. It also could be shifted by SRW left or right, and this searched-for effect would also be displayed in the image [12].

profiles to Gaussian profiles [9]. Bunch-length measurements using these techniques have been reported previously from the A0 facility [10] and FAST streak-camera system commissioning at 20 MeV [11]. Here, the focus is on the observation of the electron distribution's centroid shift *within* a micropulse and the projected transverse (spatial) and longitudinal (temporal) sizes. The temporal calibration factor was 0.20 ± 0.03 ps/pixel on the fastest streak deflection range, and the effective spatial calibration factor was 6.6 μm/pixel in the digital readout camera.

C. The all-mirror optical transport aspects

One of the challenges of using OTR is that the light yield of the mechanism is low, typically about 1% of the light in the visible regime from a 100-μm-thick YAG:Ce crystal. Of course, for picosecond-resolution imaging experiments, the ~10-fs emission time of OTR compared to the 80-ns decay time of the crystal is a critical advantage. For streak-camera work, we improved our statistics by using broadband OTR and summing micropulses and streak-camera images as stated above. To reduce the chromatic temporal dispersion effects in the streak camera due to imaging with broadband OTR, we employed a 15-m-long, all-mirror optical transport line from the beam station to the streak camera located in a light-tight box outside of the accelerator enclosure as shown in Fig. 3 and as described previously [13]. It began with an off-axis parabolic metal mirror of 178 mm focal length to capture the OTR at the port and to make the light rays parallel, and then a series of flat mirrors transported the light through the optical and terahertz instrumentation system (OTIS) box and to the streak camera. We also implemented the Hamamatsu all-mirror input optics assembly on the streak camera. This reduced the chromatic

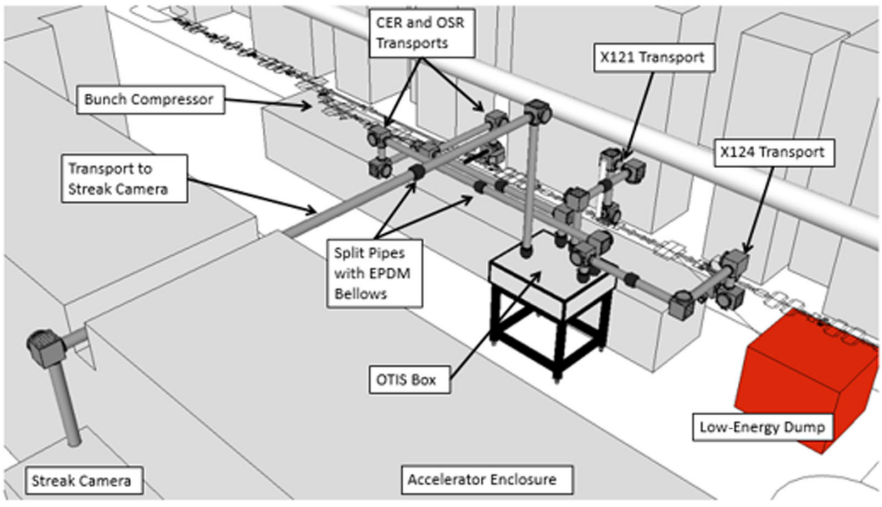

FIG. 3. Schematic of the all-mirror optics transport lines from the X121 station to the streak-camera enclosure outside of the shielding walls [13].

temporal dispersion effects of about 6 ps from the normal UV-visible multilens optical assembly to ~1.5 ps if broadband OTR were used. Normally, we use a 500-nm longpass filter to reduce the chromatic temporal effects further to the subpicosecond level [11]. Since in this case we needed as many photons as possible and the chromatic resolution term was controlled, we did not use this filter. We have only the quartz window at the beam-line cross and air in the transport line contributing to chromatic temporal dispersion. There is a final focusing mirror before the entrance slit of the streak-camera optics. The system resolution was still $\sigma < 2$ ps, which is 5 times smaller than the nominal 10-ps bunch lengths. This allowed for the temporal slicing of the micropulse distributions.

III. EXPERIMENTAL RESULTS

The experimental results are dominated by the streak-camera results, which display the head-tail-kick phenomena as well as a slice-emittance dilution effect at the tail of the pulse. We also show a comparison to the HOM submacropulse centroid oscillation effect [2] under these conditions which are shown to be too small to explain our present effects.

A. Initial streak-camera data: As-found steering and corrected steering

In order to investigate the short-range wakefield-driven submicropulse effects, we used the HOM detector signals as a measure of the transverse offset from the central axis of each of the SCRF capture cavities. Since the beam line was initially tuned with only the response-based tuning application, the as-found HOM signals in both CC1 and CC2 were nominally high. We initially identified a y-t effect in the streak-camera image under these conditions as shown in Fig. 4(a). The head of the pulse is lowest in the image, so later time is upward. The projected bunch length is $\sigma = 11.2 \pm 0.5$ ps. The transport optics rotated the image 90°, mapping the vertical (y) spatial information to the horizontal *display* axis as indicated. The temporal slices are shown in Fig. 5(a) for the head and tail of the pulses, while Fig. 5(b) shows the Gaussian fits to three such profiles with a clear $+343 \pm 15$ μm shift of the centroid from the head (blue solid curve) to the tail (red dashed curve). The projected y size was 548 ± 15 μm seen in the focus image and from Fig. 4(a). Based on the elevated HOM signals, we attributed the SRW effects to a combination of both CC1 and CC2 wakefields. The HOM detector values for CC1 US and DS and CC2 US and DS were −100, −60, −100, and −45 mV, respectively, consistent with ~1.5- to 1.0-mm offsets with an angle in both cavities.

We steered the beam with the V103 corrector by ±2.4 A from the reference, or ±5 mrad, to evaluate the effects of CC2's wakefields. Interestingly, the +5 mrad nearly doubled the head-to-tail centroid shift to $+693 \pm 20$ μm in Figs. 6(a) and 6(b), while the −5 mrad steering appeared to result in compensation of the CC1 effect and reduction of the CC2 kick, reducing the centroid shift to −55 μm as shown in Fig. 6(d). The projected beam size was also reduced by 16% compared to the as-found case and 38% as compared to the +5 mrad case as shown in Table II. The third case shows a reduced head-tail kick, but there is a crescentlike centroid shift (similar to Ref. [3] with kick compensation). The middle time sample has a shift of −184 μm, and the total projected beam size is larger than that of our more ideal case in Fig. 4(c).

In the next step, we used the H/V101 correctors before CC1 and H/V103 correctors before CC2 to minimize the four HOM signals at 500 pC/b and with 150 b. We obtained the focus-mode image in Fig. 4(b) ($\sigma_f = 3.8 \pm 0.2$ pixels) and observed an elliptical beam in y-t space as shown in Fig. 4(c) as would be expected for a space-charge-dominated regime at the rf gun photocathode. In this case, the laser spot size was ~0.2 mm as in the previous set. Also, we observed almost no y-t tilt during the micropulse [Fig. 4(c) and case 4 in Table II], so this was a preferred way to steer with the four HOM signals low at −13, −10, −5, and −7 mV. The projected y

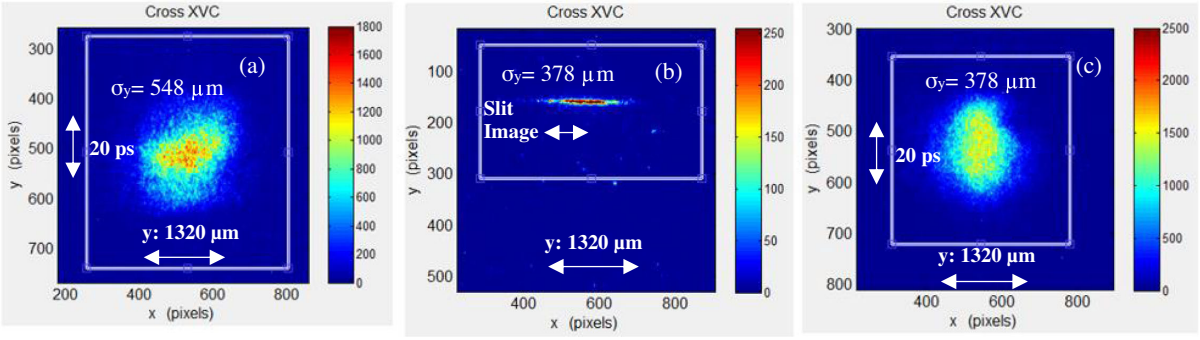

FIG. 4. (a) OTR streak-camera y-t image at X121 with HOMs as found for run 1. (b) OTR focus mode image for the corrected steering, and (c) OTR streak-camera y-t image at X121 that exhibits an elliptical-shape effect with HOMs minimized using the H/V101 and H/V103 correctors. These streak-camera data are ten-image averages. The projected y sizes are shown for all three images with the as-found case 40% larger than (c). The spatial and temporal scales are provided by the arrow heads. Pseudocolor intensities are shown in the vertical bars at the right of each image.

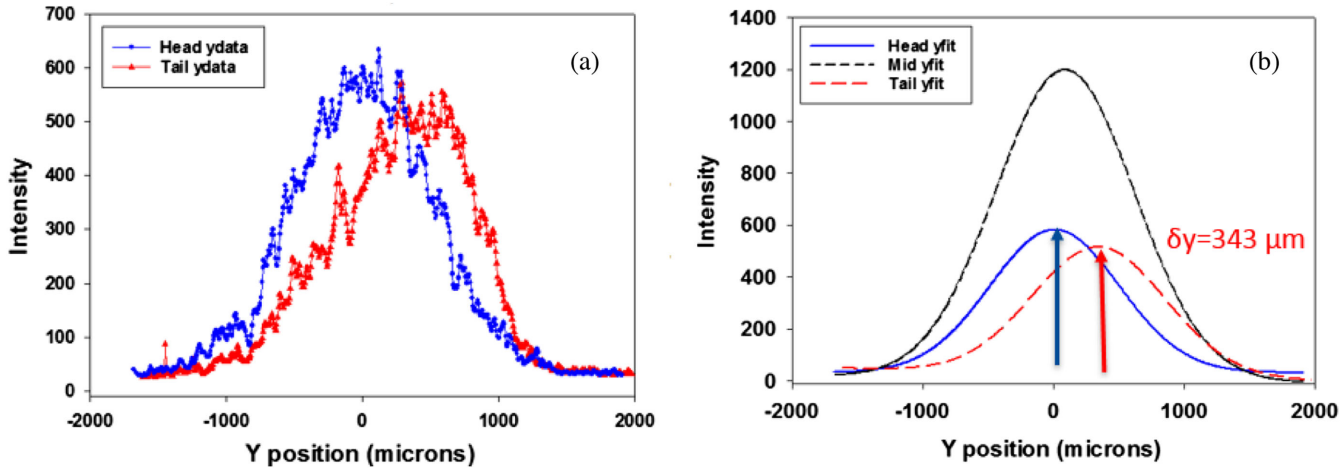

FIG. 5. (a) Transverse y profiles from the head and tail of the Fig. 4(a) Image as found. (b) Gaussian fits to the transverse profiles taken at the head, middle, and tail of the longitudinal distribution. A head-to-tail centroid shift $\delta y = +343 \pm 15$ μm was observed as indicated.

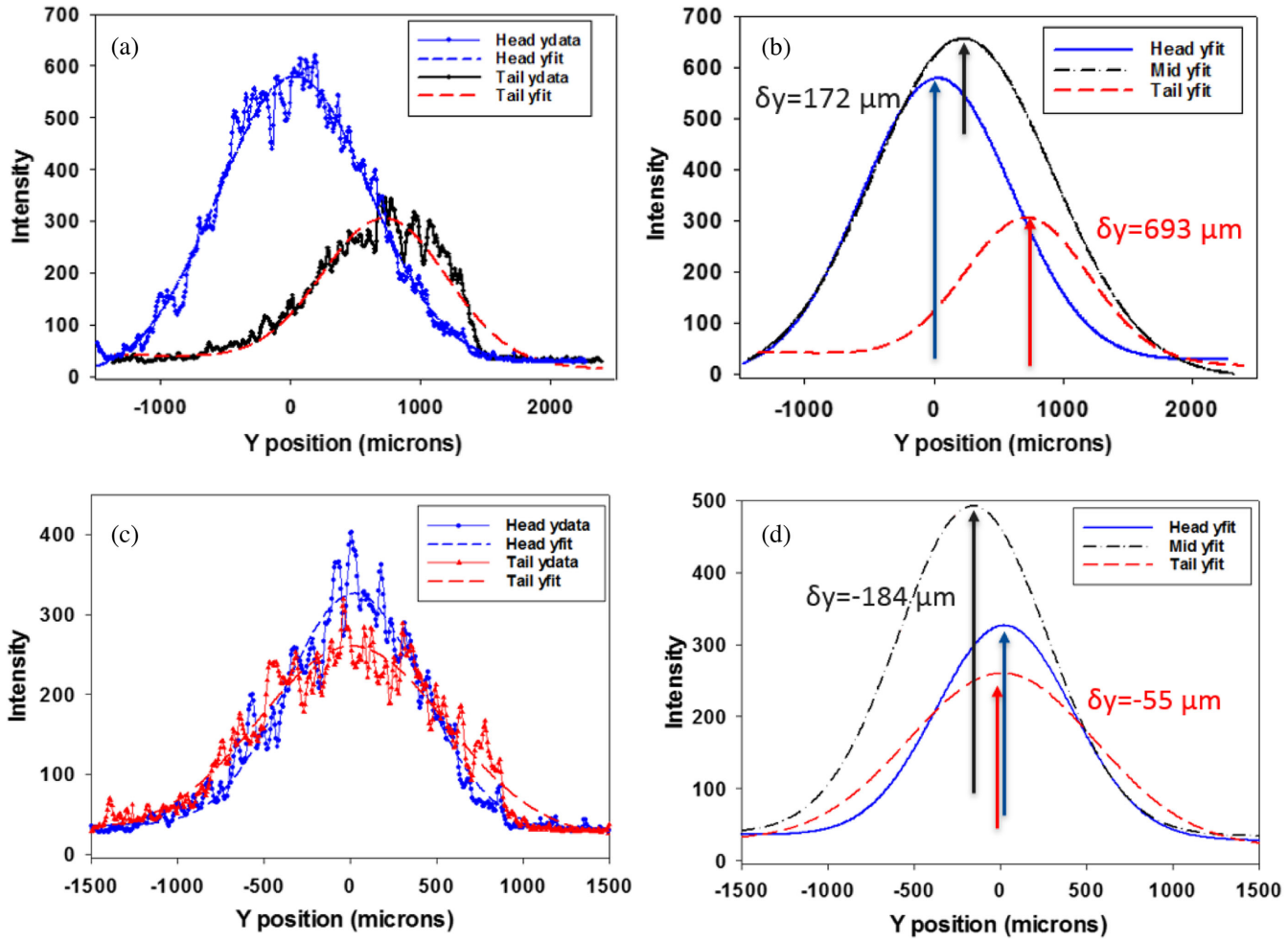

FIG. 6. (a) Transverse profiles from the head and tail of the image with V103 = +2.4 A (5 mrad). (b) Gaussian fits to the transverse profiles taken at the head, middle, and tail of the longitudinal distribution. Head-to-middle and head-to-tail centroid shifts, $\delta y = +172$ and $+693$ μm, respectively, were observed. (c) Transverse profiles from the head of the image (blue curve) with a Gaussian fit (blue short-dashed curve) and from the tail of the image (red curve) with a Gaussian fit (red dashed curve) to it for the V103 = −2.4 A (−5 mrad) case. (d) Gaussian fits to the transverse profiles taken at the head, middle, and tail of the longitudinal distribution. A head-to-tail centroid shift of only $\delta y = -55$ μm was observed for this case.

TABLE II. Summary of cases, V103 values, head-tail (H-T) centroid shifts, projected y sizes, and HOM detector signal values. Case 4 is with the HOMs and SRW minimized. The statistical errors for the spatial parameters are <5% unless provided.

Case	V103 (A)	H-T shift (μm)	Projected y size (μm)	CC1 US (mV)	CC1 DS (mV)	CC2 US (mV)	CC2 DS (mV)
1	0.43	343	548	−100	−60	−100	−45
2	+2.4 delta	693	643	−100	−55	−204	−40
3	−2.4 delta	−55	466	−100	−58	−214	−105
4	0	4 ± 4	378	−13	−10	−5	−7

size is 378 ± 10 μm in both the focus mode image in Fig. 4(b) and the streak image in Fig. 4(c), ~30% smaller than that in Fig. 4(a). This comparison provides evidence that beam size and therefore emittance dilution occurred in the "as-found" case 1 due to short-range wakefields. We were able to mitigate this with steering.

B. Wakefields and HOMs minimized: 1.2-mm laser spot size

Data were also obtained with the laser spot size of 1.2-mm rms at the virtual cathode. Our HOM signal minima were not as low as in Fig. 4(b) with 500 pC/b, but we did observe a teardrop shape as shown in Fig. 7(a). The Gaussian fit of the beam-size profile at the tail was much smaller than at the head, with no head-tail centroid shift. However, when we steered with V103 = −2 A (−4 mrad) from the reference, we observed a clear −106-μm head-tail centroid shift and a large 139-μm profile size growth from the initial 224–363 μm at the tail. This would indicate that significant dilution of slice emittance in the tail had occurred. The kick displacement result using a constant offset of 3 mm in the model is consistent with the observed shift of ~100 μm due to a nonconstant offset of ~2–4 mm in the experiment. The model assumes a constant offset from the center of the cavity which is an idealization, since the cavity fields have focusing effects. Moreover, we steered with a single corrector magnet for entrance-angle variation into CC2.

C. Bunch-by-bunch rf BPM data and LRW effects

We also evaluated the potential LRW effects on the beam centroids by using the rf BPM data and using corrector V103 before CC2. An example of the bunch-by-bunch centroid motion within the 50-micropulse train is shown in Fig. 8, where the data have been averaged over 100 macropulses. The ~100-kHz oscillation seen in the B117 data with both ±2 A (±4 mrad) is a difference frequency between HOM mode 14 in CC2 and a beam harmonic based on our earlier studies [2]. The field oscillations kicked different micropulses varying amounts, depending on the amplitude of the LRW at that point in time and the polarity of the corrector. The quadrupole triplet Q118–120 was used to focus the beam leaving the vertical size at ~800 μm at the X121 station. The vertical beam oscillation amplitude due to the near resonance with mode 14 is reduced to <20 μm for ~5 bunches at both ends of the pulse train (and even less for the 40 b in the middle of the train) at B121/X121 downstream of these quadrupoles.

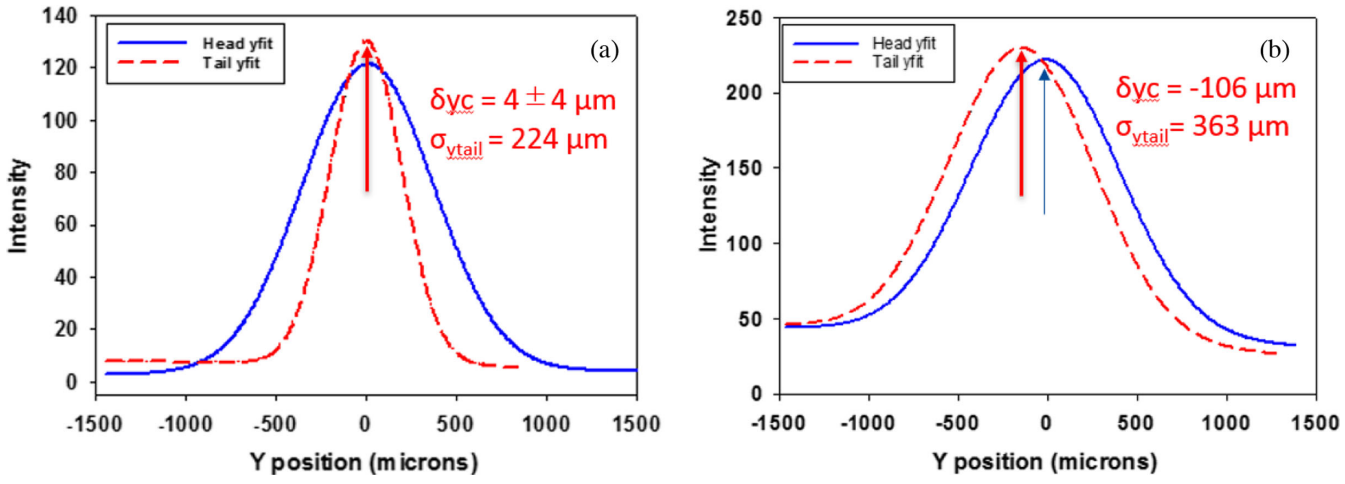

FIG. 7. (a) Comparison of the Gaussian fits to the profile taken at the head and the tail of an image with HOMs minimized and a laser spot of 1.2 mm rms. (b) Comparison of the Gaussian fits to the profile taken at the head and the tail of an image with V103 = −2 A (−4 mrad) from the reference. A clear centroid shift of −106 μm is seen, and a >50% larger profile of 363 μm at the tail is seen than in (a).

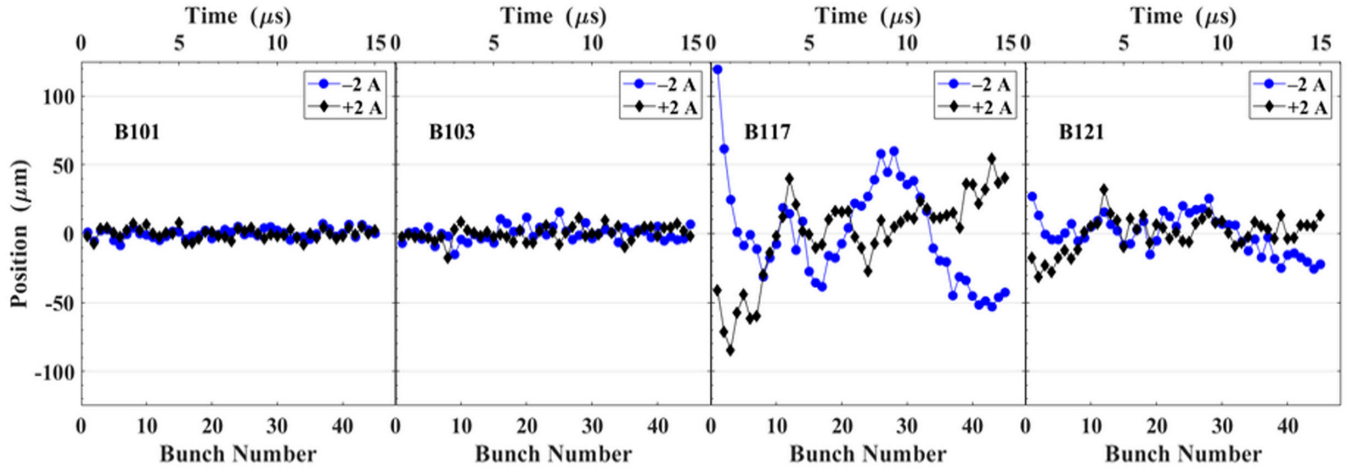

FIG. 8. Examples of the variation of the beam vertical centroids bunch by bunch for 50 micropulses and 500 pC/b at B101, B103, B117, and B121 for V103 settings of ±2 A (±4 mrad) from the reference. These were 100-shot averages to show the potential 100-kHz oscillation effects generated in CC2 when beam is off axis and observed downstream at B117 and B121. Note that no oscillations are observed in the upstream B101 and B103 locations.

Note that no oscillations are observed in the locations B101 and B103, upstream of CC2. Thus, the main competing mechanism identified for centroid motion does not account for the observed y-t effect in the 50-b summed streak image. We attribute the 100-μm head-tail effects seen in Fig. 7 to predominately short-range wakefields.

IV. NUMERICAL MODEL OF SRW IN A TESLA CAVITY

The feasibility of the measurements of the SRW effects in the Tesla cavity was evaluated using a numerical model of a single cavity. The transverse wake $W_T(s)$ for the Tesla cavity may be approximated by Eq. (1). It is based on a single-cavity wake function [14] and was additionally adjusted to fit numerical simulations of a Tesla-type nine-cell cavity. Here, $N_{\rm cell}$ is the number of cells in a cavity, a is the cavity bore radius, g is the cell length, the longitudinal wake $\gamma_{\rm eff}$ is a fitting parameter, and s is the distance between leading and trailing charges [15,16]. Parameters for our model cavity are $N_{\rm cell} = 9$, $a = 3.1$ cm, $g = 11.511$ cm, and $\gamma_{\rm eff} = 0.9 \times 10^2$:

$$W_T(s) = \frac{4N_{\rm cell}}{\pi a^3}\left\{\frac{5}{4}\left[\sqrt{2g\left(s+\frac{a}{\gamma_{\rm eff}}\right)} - \sqrt{2g\frac{a}{\gamma_{\rm eff}}}\right] - s\right\}. \quad (1)$$

The transverse kick angle $\theta_{\rm tr}(s)$ is then given by

$$\theta_{\rm tr}(s) = \frac{e_{\rm conv} e_{\rm SGS} N_e}{P_0} d \int_s^{10} W_T(s_p - s) f(s_p) ds_p, \quad (2)$$

where $e_{\rm conv} = 299.79$, $e_{\rm SGS} = 4.802 \times 10^{-10}$, N_e is the number of electrons, P_0 is the momentum in eV, d is the offset, and s_p is the position along the bunch. The submicropulse transverse kick angles of 5–10 μrad in the tail of the pulse shown in Fig. 9(a) were calculated for an

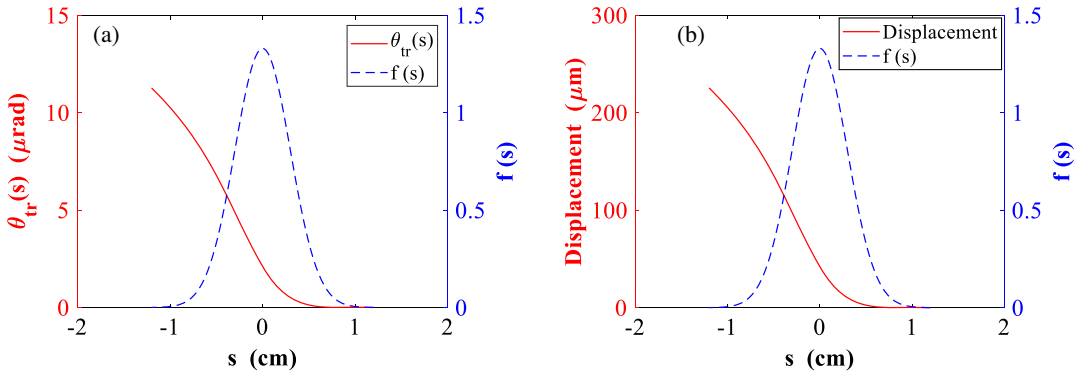

FIG. 9. (a) Plot of the s-dependent kick angle in microradians (red) within the 10-ps-long micropulse (blue curve) for a 500-pC charge, a 5-mm offset, and 33 MeV. (b) Plot of the s-dependent transverse displacement in microns (red) with $M_{12} = 20$ m.

initial case of $Q = 0.5$ nC, $\sigma_s = 3$ mm, offset $= 5$ mm, the transport matrix element $M_{12} = 20$ m, and the energy in the middle of CC2 $= 33$ MeV. The $4\sigma_s$ lengths of ± 12 mm around the center point were split into $N = 40$ samples with $s_n = s_{\min} + (s_{\max} - s_{\min})xn/N$, $n = 0$ to $N - 1$. There would be a corresponding s-dependent displacement kick of 100–200 μm in the tail of the pulse as shown in Fig. 9(b) [16]. We were able to steer the beam off axis up to 10 mm in CC1 and 5 mm in CC2 using the correctors as shown in the previous work [2] to excite the transverse wakefields. SRW effects should be linear with charge, offset, and M_{12}. When we scale these results to a 3-mm offset, they are representative of the single-cavity effects observed for CC2 in Sec. III B.

V. SUMMARY

In summary, a series of observations of short-range wakefield effects from a Tesla cavity was made for the first time using a synchroscan streak camera to obtain y-t images at the submicropulse timescale. The HOM detectors and rf BPMs were used to evaluate off-axis steering in the two cavities related to these tests, and the HOM-induced submacropulse centroid motion was shown to be much smaller than the observed submicropulse head-tail centroid shift effects. In addition, we demonstrated compensation of the SRW kicks from CC1 by steering differently into CC2 and mitigation of the beam size and concomitant emittance dilution at FAST by steering on axis for minimized HOM signals. These results could be extendable to cryomodules. Moreover, the head-tail centroid kicks observed of $\sim$100 μm in CC2 were consistent with a short-range wakefield model for the single Tesla-type superconducting rf cavity and attributed to that effect. Because the kick angle is inversely proportional to the beam energy, such effects on slice and projected emittance dilution should be considered on beams injected into a Tesla cavity at a lower energy. Examples are $\sim$4.5 MeV at FAST, the European XFEL injector, the conceptual linear collider injector, and especially $\sim$1 MeV for the LCLS-II injector [17]. We suggest that these data could be used to benchmark simulation codes and applied to cryomodule configurations in advanced accelerator facilities.

ACKNOWLEDGMENTS

The authors acknowledge the support of C. Drennan, A. Valishev, D. Broemmelsiek, G. Stancari, V. Shiltsev, S. Nagaitsev, and M. Lindgren, all in the Accelerator Division at Fermilab. We also specifically acknowledge V. Lebedev (Fermilab) for the Tesla cavity SRW numerical results reported here and V. Yakovlev (Fermilab) for discussions on wakefields in Tesla cavities. This manuscript has been authored by Fermi Research Alliance, LLC under Contract No. DE-AC02-07CH11359 with the U.S. Department of Energy, Office of Science, Office of High Energy Physics.

[1] W. K. H. Panofsky and M. Bander, Asymptotic theory of beam break-up in linear accelerators, Rev. Sci. Instrum. **39**, 206 (1968).

[2] A. H. Lumpkin, R. Thurman-Keup, D. Edstrom, J. Ruan, N. Eddy, P. Prieto, O. Napoly, B. E. Carlsten, and K. Bishofberger, Submacropulse electron-beam dynamics correlated with higher-order modes in Tesla-type superconducting rf cavities, Phys. Rev. Accel. Beams **21**, 064401 (2018).

[3] A. H. Lumpkin and M. Wilke, Time-resolved electron-beam characterizations with optical transition radiation, Nucl. Instrum. Methods Phys. Res., Sect. A **331**, 803 (1993).

[4] J. T. Seeman *et al.*, Transverse wakefield control and feedback in the SLC linac, SLAC National Accelerator Laboratory Report No. SLAC-Pub-4182, 1987.

[5] H. Weise, Commissioning and first lasing of the European XFEL, in *Proceedings of the 38th International Free Electron Laser Conference* (JACoW, Geneva, 2017), MOC03.

[6] P. Emma, Status of the LCLS-II FEL project at SLAC, in *Proceedings of the 38th International Free Electron Laser Conference* (JACoW, Geneva, 2017), MOD01.

[7] The ASTA User Facility Proposal, Fermi National Accelerator Laboratory Report No. Fermilab-TM-2568, 2013.

[8] J. Ruan, M. Church, D. Edstrom, T. Johnson, and J. Santucci, Commission of the drive laser system for the advanced superconducting test accelerator, in *Proceedings of the 4th International Particle Accelerator Conference, IPAC-2013, Shanghai, China, 2013* (JACoW, Shanghai, China, 2013), WEPME057.

[9] R. Thurman-Keup, FNAL, off-line MATLAB-based ImageTool, 2011.

[10] A. H. Lumpkin, J. Ruan, and R. Thurman-Keup, Synchroscan streak camera imaging at a 15-MeV photoinjector with emittance exchange, Nucl. Instrum. Methods Phys. Res., Sect. A **687**, 92 (2012).

[11] A. H. Lumpkin, D. Edstrom, and J. Ruan, Initial demonstration of 9-MHz framing camera rates, in *Proceedings of the 2016 North American Particle Accelerator Conference* (JACoW, Geneva, 2016), TUPOA25.

[12] B. X. Yang (private communication).

[13] R. Thurman-Keup, A. H. Lumpkin, and J. Thangaraj, An optical and terahertz instrumentation system at the FAST linac at Fermilab, in *Proceedings of the 2017 International Beam Instrumentation Conference* (JACoW, Geneva, 2017), WEPCC04.

[14] A. V. Novokhatski, On the estimation of the wake potential for an ultrarelativistic charge in an accelerating structure, Report No. 88-39, Institute of Nuclear Physics, Novosibirsk, 1988.

[15] T. Weiland and I. Zagorodnov, The short-range transverse wake function for Tesla accelerating structure, Tesla Report No. 2003–19.

[16] V. Lebedev (private communication).

[17] F. Zhou, D. H. Dowell, P. Emma, J. Schmerge, C. Mitchell, and F. Sannibale, LCLS-II injector physics design and beam tuning, in *Proceedings of the 2017 International Particle Accelerator Conference* (JACoW, Geneva, 2017), TUPAB138.